The effect of the Region 2 currents location on the strength of the auroral electrojet and global distribution of ionospheric currents

Sonya Lyatsky[1] and Natalia Buzulukova[2]

[1]Catholic University of America
[2]NASA GSFC - University of Maryland,Moscow Institute of Physics and Technology,Moscow Space Research Instititute (IKI)

November 23, 2022

Abstract

In this study, we use a parametrized model of ionospheric electrodynamics to investigate the effect of Region 2 currents' location on the development and dynamics of the auroral electrojet (AE), using real cases data as input parameters for our simulations. We calculated the maps of equivalent ionospheric currents reproducing the events of interest, analyzed the results and compared with SuperMAG observations. The simulations have shown that strong R2 currents provide a robust closure for the ionospheric currents flowing from R1 via auroral zone ionosphere. We found that the highest magnitude westward auroral electrojet is in the day-to-dawn sector, while the equivalent ionospheric currents on the night-side have much lower magnitude. We suggest that the location of the R2 currents affects the entire distribution of ionospheric currents, changing the MLT location and magnitude of the maximum auroral electrojet. As the distance between the location of the maxima for the R1 and R2 current systems increases, the magnitude of the ionospheric currents decreases because the ionospheric currents spread over larger regions at low latitudes. When R2 currents cannot provide the proper closure, the ionospheric currents flow from the dawn to dusk over the night-side ionosphere, leading to the westward auroral electrojet development in the night region of the auroral zone. We analyzed features and magnitude of these currents and compared with observations.

Hosted file

`essoar.10505208.1.docx` available at https://authorea.com/users/545057/articles/601906-the-effect-of-the-region-2-currents-location-on-the-strength-of-the-auroral-electrojet-and-global-distribution-of-ionospheric-currents

1 **The effect of the Region 2 currents location on the strength of the auroral**

2 **electrojet and global distribution of ionospheric currents**

3 **S. Lyatskaya[1,3], N. Buzulukova[2,3]**

4 [1] Catholic University of America

5 [2] University of Maryland, College Park

6 [3] NASA Goddard Space Flight Center

7 Corresponding author: Sonya Lyatskaya (lyatskys@cua.edu)

8

9 **Key Points:**

10 • Strong R2 currents provide robust closure for the ionospheric currents flowing from R1

11   system via auroral zone ionosphere.

12 • MLT distribution and strength of the auroral electrojet is sensitive to the R2 currents,

13   with weaker and broader electrojet for more equatorial R2 location.

14 • Simulations show close characteristics to the observed events but also suggest to consider

15   additional factors including substorm current wedge and auroral potential drop.

16

17

18   **Abstract**

19   In this study, we use a parametrized model of ionospheric electrodynamics to investigate the

20   effect of Region 2 currents' location on the development and dynamics of the auroral electrojet

21   (AE), using real cases data as input parameters for our simulations. We calculated the maps of

22   equivalent ionospheric currents reproducing the events of interest, analyzed the results and

23   compared with SuperMAG observations. The simulations have shown that strong R2 currents

24   provide a robust closure for the ionospheric currents flowing from R1 via auroral zone

25   ionosphere. We found that the highest magnitude westward auroral electrojet is in the day-to-

26   dawn sector, while the equivalent ionospheric currents on the night-side have much lower

27   magnitude. We suggest that the location of the R2 currents affects the entire distribution of

28   ionospheric currents, changing the MLT location and magnitude of the maximum auroral

29   electrojet. As the distance between the location of the maxima for the R1 and R2 current systems

30   increases, the magnitude of the ionospheric currents decreases because the ionospheric currents

31   spread over larger regions at low latitudes. When R2 currents cannot provide the proper closure,

32   the ionospheric currents flow from the dawn to dusk over the night-side ionosphere, leading to

33   the westward auroral electrojet development in the night region of the auroral zone. We analyzed

34   features and magnitude of these currents and compared with observations.

35   **Plain Language Summary**

36   Solar wind is a stream of charged particles flowing from the Sun in all directions. When they

37   reach planets with magnetic fields, like our Earth, they interact with these magnetic fields

38   creating magnetosphere, which is similar to a magnetic bubble around the planet. Due to the

39   interaction between the solar wind particles and Earth's magnetic field, a giant loop of current is

formed in space that circulates between the solar wind, the magnetosphere and the Earth's

ionosphere. These currents could sometimes cause the most spectacular phenomenon, Aurora

Borealis in the Northern hemisphere, and Aurora Australis in the Southern. These auroras have

distinctive ring-shaped structures that form around the polar caps. These formations are called

auroral ovals or auroral zones. The auroras occur in the same place where the most intense

currents flow, therefore it is important to understand the interactions between current systems

and their ionospheric closures. The Region 1 currents appear at the inner (high geomagnetic

latitudes) boundary of the auroral oval, and Region 2 currents appear at the outer (low

geomagnetic latitudes) boundary of this oval. The interactions between these Region 1 and 2

currents occurs via highly conductive auroral oval, where observations of ionospheric currents

provide information about the currents closure. Using numerical simulations and comparison

with the observations, we studied how the location of R2 currents affects the development and

dynamics of the ionospheric currents during geomagnetic disturbances, including geomagnetic

substorms.

1. Introduction

The global three-dimensional magnetosphere-ionosphere current system is one of the most

important phenomena in the Earth's environment. The interaction of the solar wind and the Earth

magnetosphere can generate a number of geomagnetic phenomena, e.g. reconnection of the

Earth's and interplanetary magnetic field (IMF) and hence convection of magnetic field lines,

ionospheric and field aligned currents (FACs), etc.

61   The magnitude of currents depends on many conditions, for example, IMF direction,

62   currents location, ionospheric conductivity, and a few others. Some of the conditions are

63   relatively stable, such as ionospheric conductivity due to solar illumination, for example the

64   sunlit regions of the ionosphere have higher conductivity due to ionization by the solar light.

65   This condition changes relatively slowly with the movement of the Earth around the Sun.

66   Some other conditions may experience rapid changes, such as the ionospheric conductivity

67   associated with auroral precipitation, the expansion and contraction of the polar cap, and the

68   boundaries of the auroral zone [e.g., Akasofu, 1964].

69   These rapidly changing conditions are usually related to the orientation of the IMF, for

70   example, the southward oriented IMF can reconnect with the Earth's magnetic field. This

71   process results in significant penetration of the solar wind into the magnetosphere, causing

72   auroras, polar caps expansion, equatorward shifting and expanding of the auroral zones, and

73   strong field-aligned and ionospheric currents. The Region 1 (R1) FACs, which emerge at the

74   polar cap boundaries, also develop at the lower latitude. The secondary FAC system, so called

75   Region 2 (R2) currents, is generated at the equatorward boundaries of the auroral zone, which

76   correspond to the plasma sheet inner boundary; these boundaries are also expanding and drifting

77   equatorward. These current systems have been extensively studied and described in various

78   articles [Iijima and Potemra, 1976; Weimer, 2001; Papitashvili et al., 2002; Anderson et al.,

79   2005, Lyatsky et al., 1974, Ganushkina et al., 2018 and references therein].

80   Over the past decade, there have been significant advances in understanding the

81   configuration, dynamics, and drivers for various current systems of the Earth's magnetosphere

82   (e.g., review of current systems by Ganushkina et al., 2018 and references therein). The DMSP,

83   SWARM, Iridium, AMPERE, MMS and CLUSTER missions allow detailed analysis of the

84   complex structure of currents, including the Region 2 currents. Ohtani et al., 2010 used DMSP

85   data to identify R1/R2 current systems and relate their boundaries to various precipitation

86   boundaries. It has been showed that the maximum energy flux for ion precipitation (b2i

87   boundary) is located inside R2 currents, and hence can be used as an identifier for R2 current.

88   Korth et al., 2014 have studied R1/R2 currents with Iridium data in order to correlate R1/R2

89   currents with auroral emissions obtained from TIMED data and found that the results are in

90   agreement with Ohtani et al., 2010. During geomagnetically active times, nightside R2 system

91   evolves as a response to substorm activity and modified by superposition with substorm current

92   wedge (Murphy et al., 2013). Since substorms ultimately brings plasma from the tail to the ring

93   current region, substorm current wedge can be viewed as an important link connecting R1/R2

94   systems during substorms (Kepko et al., 2015). An important interplay between global R1/R2

95   systems is established in Anderson et al., 2018. It has been found that R1 system do not fully

96   develop without R2 currents; they intensify together first at dayside, and then at nightside after

97   the onset of activity.

98   R2 currents have been successfully modelled over the past two decades using so-called ring

99   current models (Zheng et al., 2006 and references therein). A ring current model calculates

100   plasma distribution in the inner magnetosphere and compute R2 currents from Vasyliunas

101   equation (Toffoletto et al., 2003, equation 12). This approach produces large scale R2 currents,

102   both upward and downward (Zheng et al., 2006). If interchange instability occurs in the inner

103   magnetosphere, the model R2 system develops a characteristic pattern consisting of intermittent

104   upward/downward currents (Sazykin et al., 2002; Buzulukova et al., 2008).

105

106   Recent simulations with global MHD model coupled with the ring current module also

107   demonstrate intermittent structure of R2 currents at nightside, resulting from the interaction of

108   magnetotail bursty flows with dipole-like inner magnetosphere (Yu et al., 2017).

109   In this paper, we investigate the role of R2 current system using a parametrized model of

110   ionospheric electrodynamics, where the location of R1 and R2 current systems is a parameter, as

111   well as the magnitude of the currents, polar boundary electric field potential and ionospheric

112   conductivity. This simplified approach is different from the sophisticated first-principles models

113   mentioned above. Being less computationally expensive, it nevertheless makes it possible to

114   disentangle important physical properties of magnetospheric current systems, often hidden in the

115   self-consistent solution.

116

2. Model Input and Simulation Results

118   In current work, we have used the previously developed model of ionospheric

119   electrodynamics (Lyatskaya et al., 2014, 2015, 2016), hereinafter L-2015, to analyze the impact

120   of the R2 currents location on the global magnetosphere-ionospheric current system. The model

121   uses as an input the location and magnitude of R1, R2 field-aligned currents, the ionospheric

122   conductivity and the polar boundary electric field potential. The model produces ionospheric

123   currents and field-aligned currents, including interhemispheric currents flowing between the

124   northern and southern conjugate ionospheres in the case of asymmetry of ionospheric

125   conductivities in two hemispheres. The model described in detail in Lyatskaya et al., 2015. For

126   the simulation, we selected the season, when the impact of interhemispheric currents would be

127   minimal.

128   One of the assumptions of the model is that the potential drop along magnetic field line in

129   the auroral region is negligible. While this assumption is not always valid, it mimics a similar

130   assumption adopted in global MHD codes with a separate module for ionospheric

131   electrodynamics. While we anticipate the importance of auroral potential drop, we assume that it

132   will not change the studied effects of R2 location quantitatively. The role of auroral potential

133   drop will be investigated in another study.

134   As input to the model, we used an electric potential distribution at the boundaries of the

135   auroral zone as boundary conditions of the simulation. The potential distribution at the polar cap

136   was taken from the Active Magnetosphere and Planetary Electrodynamics Response Experiment

137   (AMPERE) data products [Anderson, et al. 2008a, 2014, and references therein]. AMPERE data

138   of the field aligned currents were used for both control purposes and as a means of defining the

139   location of the R1 and R2 currents. We adopted Hardy et al. [1987] [see also Weimer, 1999]

140   model for ionospheric conductivity for Kp=4 and 5. The 3-hour magnetic activity index, Kp,

141   [Bartels, 1949] is broadly used because this index reflects the large-scale features of various

142   levels of geomagnetic activity, which generally include electric potential drop across the polar

143   caps, ionospheric conductivity magnitudes of both types, Hall and Pedersen, and others.

144   For control of simulation results and comparison with the observations, we used SuperMAG

145   polar plots with ground magnetometers vectors, which represent equivalent ionospheric currents

146   [Gjerloev, (2012), Waters, et al. (2015), and references therein].

147   To better understand the role of R2 currents and their effect on the entire ionosphere-

148   magnetospheric current system, we performed several simulations with L-2015 model by

149   choosing a simulation setup close to the selected real cases. We selected some of the cases to

150   demonstrate the role of R2 currents in the magnetospheric substorm development.

151   We also compared the observations with the result of the simulation. First, we considered a

152   moderate substorm on April 6, 2010 around 21:10 UT. The AU and negative AL indices are

153   shown in the Figure 1, upper panel, and the components of the interplanetary magnetic field with

154   steady negative Bz are shown in the lower panel. The pink shade indicates a time-zone of interest

155   around 21:10 UT, though there is a time delay between certain IMF parameters and AE indices

156   they produce.

157   Figure 2 shows the reconstructed electric field potential (a) and field-aligned current density

158   (b) derived from the AMPERE data products for April, 06, 2010, 21:10 UT, and SuperMAG

159   polar plots (c) with ground magnetometers vectors, which represent the equivalent ionospheric

160   currents for the Northern (left) and Southern (right) hemispheres during the same period. The

161   southern hemisphere is shown as a mirror image. For all AMPERE, SuperMAG and L-2015

162   simulation polar plots, the direction toward the Sun (12 MLT) is above each plot, and toward

163   dawn (06 MLT) is on the right.

164   Equivalent ionospheric currents should not be mixed with real ionospheric currents. Ground

165   magnetometers register magnetic variations, which are produced by two major currents systems:

166   field-aligned currents and ionospheric currents. In the ground-based magnetometers data, we

167   cannot separate these two effects. Therefore, for convenience, the observations could be

168   interpreted as a result of flow of an imaginary ionospheric current system, with zero field-aligned

169   currents. These equivalent ionospheric currents are defined as the divergence-free ionospheric

170   current distribution, which produce the same magnetic field below the ionosphere as the original

171   currents consisting of ionospheric and field-aligned currents [e.g., Fukushima, 1976; Kamide et

172   al., 1981; Matsushita and Xu, 1982; Lyatsky and Maltsev, 1983; Amm and Viljanen, 1999;

173   Weygand et al., 2012, and references therein]. These divergence-free equivalent ionospheric

174 currents are very convenient way to represent the spatial distribution of geomagnetic

175 disturbances under the ionosphere, and our model allows this distribution to be calculated.

176   From the AMPERE images, Figure 2 (b), the R1 currents are visibly localized around 17º-

177 18º of colatitude, while the location of weak R2 currents is around 26º. However, the same time,

178 the SuperMAG images Figure 2 (c) show strong equivalent ionospheric currents reaching 30º

179 colatitude of the auroral zone. Therefore, we made simulations for several different locations of

180 R2 currents up to 30º colatitude.

181   For the first simulation we used the parameters of the event described above. The R1

182 currents location is set for 18º of colatitude, the R2 currents are on 26º. The total ionospheric

183 conductivity is defined by two major factors: solar illumination and auroral precipitation

184 [Lyatskaya et al. 2015 and references therein], which parameters are typical for KP = 4, e.g. the

185 maxima of Pedersen and Hall conductivities are respectively 10.0 S and 18.0 S (after Hardy et al.

186 [1987]). The electric field potential drop for the boundary conditions was taken from the

187 AMPERE product (MIX ionospheric solver); it changes from -30 kV at the eastern boundary of

188 the polar cap (18 MLT) to +42 kV at the western boundary (06 MLT). It should be noted that

189 only potential drop is taken from MIX ionospheric solver, and the total potential distribution in

190 the auroral zones was derived from the solution of the 3-D continuity equation for the currents in

191 both ionospheres with Hardy model of ionospheric conductivity, as described in [Lyatskaya et al.

192 2015].

193   Figure 3 shows the electric field potential simulated with L-2015 for given boundary

194 conditions and ionospheric conductivities in two hemispheres for the described case

195 configuration. The calculated potential distribution is close to the results of the MIX model in the

196 AMPERE products. Figure 4 shows the simulated equivalent ionospheric currents, for the

197   Northern (left) and Southern (right) hemispheres for the above case. The results of the simulation

198   are as follows: the AU index is 929 and 895 nT for the northern and southern ionospheres; the

199   AL index is -963 and -926 nT respectively. The magnitude of the indices is very close to the

200   observational data (Figure 1 b), where we can see that the AU index in this time frame fluctuates

201   between 800 and 1000 nT, and the AL index fluctuates between -600 and -800 nT.

202   For this model setup, the simulated electric field potential distribution (Figure 3) is very

203   close to the AMPERE potential distribution shown on Fig. 2 a, but the equivalent currents maps

204   Fig. 4 (bottom) differ significantly from Figure 2 (c): the SuperMAG plot shows a strong

205   equivalent ionospheric current on the night side, while the simulated equivalent ionospheric

206   currents decrease significantly from dawn side toward the night side. The strongest simulated

207   westward electrojet current is in the day-to-dawn sector, with the strongest simulated eastward

208   electrojet current being in the day-to-dusk region.

209   The obvious explanation for the reduction in ionospheric currents on the night side is that

210   these currents flow across the auroral zone rather than along it. The highly conductive auroral

211   zone of the ionosphere provides a robust connection between the R1 and R2 currents. To better

212   understand this effect, the following simulation was performed for the same set of parameters

213   except that the R2 current location was set to 28° colatitude. The AU indices for this simulation

214   are 744 and 714 nT for Northern and Southern hemispheres respectively, and the AL indices are

215   -769 and -737 nT. Increasing the distance between the location of R1 and R2 currents results in a

216   widening of the region of the equivalent ionospheric currents and a decrease in their magnitude.

217   Further displacement of R2 currents to a lower colatitude, e.g. 30° (Figure 5), leads to an even

218   greater decrease in the magnitudes of the equivalent ionospheric currents, as well as in the AL

219   and AU indices. In this case, the AU reduces to 610 and 583 nT for the Northern and Southern

220   ionospheres respectively; AL index changes to -626 and -598 nT for the same hemispheres.

221   Moving R2 even further away from the R1 currents results in further reducing the magnitude of

222   the equivalent ionospheric currents. However, the ionosphere still provides a connection between

223   the R1 and R2 currents, and the ionospheric currents in the night sector will never reach the

224   magnitude of SuperMAG data.

225   There is one more scenario which produces a westward auroral electrojet in the model

226   through the night side to bring it closer to the SuperMAG data. This is the set of parameters, for

227   which R2 currents are absent or small in magnitude, as well their shielding effect. This scenario

228   is supported by AMPERE data, because the R2 currents around the period of interest are low in

229   magnitude. The absence of intense R2 current means that their shielding effect is weak. In terms

230   of auroral electrodynamics, the shielding effect on inner boundary of the plasma sheet

231   determines the penetration of the electric field from the auroral zone to the lower latitude. In the

232   context of inner magnetosphere models, the shielding effect from R2 currents was studied in

233   numerical simulation by Jaggi and Wolf [1973] and analytically estimated by Maltsev [1974]. It

234   is also routinely reproduced in ring current simulations. It has been shown with CRCM

235   simulations of the ring current dynamics (Fok et al., 2010), that the shielding becomes weaker in

236   the case of dynamic magnetic field variations (see Figure 3 from Fok et al., 2010). The April 6,

237   2010 event is characterized by intense and continuous auroral activity, so-called HILDAA events

238   (Tsurutani et al., 2009, Hajra et al., 2013). The continuous auroral activity is likely causing

239   magnetic field variations in the near-earth plasma sheet, and therefore weakens the shielding

240   with a weakened R2 current system. AMPERE data confirms that the R2 currents are weak

241   during the event of interest, despite strong auroral activity. It is important to note that the Dst_{min}

242   was equal -79 nT during the day, indicating the development of only a moderate geomagnetic

243   storm.

244   When R2 currents are weak, they cannot provide closure of the ionospheric currents. This

245   closure is provided by the auroral zone ionosphere, and under certain conditions by

246   interhemispheric currents. This mode was discussed and simulated in [Lyatskaya, et al. 2016];

247   the simulation showed appearance of a strong westward auroral electrojet in the night side

248   [Benkevich et al., 2000; Benkevich and Lyatsky, 2000; Lyatskaya et al., 2014, 2015, 2016].

249   However, the interhemispheric currents appear when there is a significant difference in

250   ionospheric conductivity between hemispheres. This difference could be substantial during

251   summer or winter season but not during spring and fall, when the two hemispheres are

252   illuminated roughly equally, and the influence of interhemispheric currents in the above cases

253   could be excluded. Therefore, in the next simulation setup we study the closure of the

254   ionospheric currents without interhemispheric currents and without R2 currents.

255

256   For this simulation, we set the R1 current location and all other parameters of the simulation

257   in the same way as in the above cases excluding only the R2 currents. The simulation showed

258   that in absence of R2 currents, there is no closure for R1 and ionospheric currents through the

259   equatorward boundaries of the auroral zone, therefore this closure is provided by the night side

260   ionosphere. However, with the above parameters, the magnitude of the equivalent ionospheric

261   current on the night side was far from observations, e.g., the AU and AL indices for the Northern

262   and Southern ionospheres are respectively: 332, 307, -310, and -312 nT.

263   To reproduce the observed values for auroral indices, we increased the electric field

264   potential drop across the polar cap for the simulation, from +105 kV to -75 kV. The outcome of

265   the simulations is shown in the Figures 6 and 7. There are predictably stronger ionospheric

266   currents and a strong westward auroral electrojet in the night sector. The AU and AL indices for

267   the Northern and Southern ionospheres are respectively: 830, 767, -776, -779 nT. In the polar

268   plots, we can observe that the equivalent ionospheric currents are now flowing along the auroral

269   oval on the night side, because the closure through R2 currents is not available.

270   The comparison between all the above cases is shown in the Figure 7. We plotted the

271   simulated with L-2015 horizontal component of the magnetic field that would be measured on

272   the ground in various sectors of the magnetic local time (MLT) of the auroral zone for the cases

273   described above. The upper (lower) magnitude of horizontal magnetic component recorded along

274   the entire auroral oval represents the AU (AL) index. These indices (Davis and Sugiura, 1966,

275   Tomita et al. 2011) show the disturbance level recorded by magnetometers located in the auroral

276   zone; they are directly related to the magnitude of equivalent ionospheric currents and therefore

277   present a convenient and widely used form of describing the level of activity.

278

279   In the Figure 7, the positive magnetic field variation is caused by the eastward auroral

280   electrojet, and its maximum represents the AU index for each hemisphere for this particular time.

281   The negative magnetic field is caused by the westward auroral electrojet, and its minimum

282   represents the AL index. The multicolored curves show the results of the simulations made for

283   the cases with the R2 currents set to 26° (red line), 28° (blue), 30° (green), and 32° (cyan). The

284   solid black curve shows the simulation result for the case where R2 currents are absent in the

285   model, but all the other parameters are the same as above. The black dashed curve shows the

286   results for the run with the R2 currents absent and the increased potential drop over the polar cap

287   (see Figure 6 for the maps of equivalent currents). The bold lines show the magnetic field

288 variation for the Northern hemisphere, and the thin lines show the results for the Southern

289 hemisphere. As the simulation is made for the spring season, the difference between the

290 magnitudes resulting from interhemispheric currents is negligible.

291   Figure 7 gives an overview in which MLT sector one can find the greatest magnitude of

292 the ionospheric currents. We also compare the model results with SuperMAG data and auroral

293 indices. As one can see, the red and blue lines for runs with R2 currents provide a good fit for the

294 AL and AU indices with observations. However, there is no model setup with strong R2 currents

295 that produces a strong westward electrojet in the midnight sector as suggested by the SuperMAG

296 data (Figure 2). The model setup, which corresponds to the observations with a strong midnight

297 electrojet, is the run without R2 currents, shown in the Figure 7 by dashed lines. This is also

298 consistent with AMPERE data, where no R2 currents appear around the simulation time. We

299 note that to obtain a strong electrojet for the model run without R2 currents, the potential drop

300 has been increased from ~75 kV to ~ 170 kV. We suggest that this discrepancy is the result of

301 several factors, including unambiguity in MIX solver solution, the effects of potential drop along

302 auroral field line and imperfect conductivity model in L-2015 model.

303

304   To further investigate the effects of R2 system on the ionospheric currents closure, we

305 analyzed another case of a magnetospheric substorm that occurred on April 5, 2010. The

306 substorm of April 5, 2010 happened after arrival at ~ 08:25 UT of CME-driven shock that

307 compressed the magnetosphere, applied Bz=-15 nT and caused a development of the extreme

308 geomagnetic substorm near 9:30 UT (Connors et al., 2011). It is believed that an unusually large

309 depolarization observed at GOES s/c at this time could be related to the Galaxy 15 s/c anomaly

310 and shows an example of space weather conditions that may have induced a major operational

311   anomaly (Connors et al., 2011). Since L-2015 does not currently include the effects of the

312   substorm current wedge, we selected for the analysis an early expansion phase around 09:10 UT,

313   where the effects of substorm current wedge are supposedly not very strong. The AU and

314   negative AL indices (top) and interplanetary magnetic field components (bottom) are shown in

315   the Figure 8. We can see that the AU and AL indices reach their maximum magnitude between

316   2000 and 2500 nT around 09:30 UT, and fluctuate in the range 1000-1500 nT around 09:10 UT.

317   There is a strong and stable southward IMF Bz component, and a strong and fluctuating By IMF

318   component around 09:10 UT.

319   Figure 9 shows the suggested electric field potential derived from MIX ionospheric solver

320   (a), field-aligned current density (b) derived from AMPERE data for April 5, 2010, 9:10, and (c)

321   SuperMAG polar plots with ground magnetometers vectors for the Northern (left) and Southern

322   (right) hemispheres. The AMPERE data does not show substorm current wedge signatures

323   around this time. The R2 currents are weak in the Northern hemisphere, but present in the

324   Southern hemisphere.

325

326   We made a set of simulations with the same approach: the R1 current location is set for 20°

327   of colatitude as follows from the AMPERE polar plots on Figure 9, the R2 location is set for 30°,

328   32°, 34°, and 36°, and also some cases were considered with R2 currents absent from the

329   simulations. The ionospheric conductivity parameters related to typical auroral precipitations for

330   KP = 5, e.g. the maxima of Pedersen and Hall conductivities are 12.5 S and 25.9 S respectively.

331   The electric potential difference for the boundary conditions was taken from the AMPERE polar

332   plot; it changes from -110 kV at the western boundary of the polar cap to +61 kV at the eastern

333   boundary (Figure 9 a). The maximum and minimum of a potential has moved from 06 and 18

334   MLT to 03 and 15 MLT respectively (as in the AMPERE data, Figure 9 a) due to strong By

335   component of the interplanetary magnetic field. The resulting potential calculated from L-2015

336   for 9:10 UT of April 5, 2010 is shown in the Figure 10. Similar to the first case, the AMPERE

337   product (MIX solver) is only used to set up the boundary condition.

338

339   We made a set of simulations setting up the R2 currents at 30º, 32º, 34º, as well as the set of

340   simulations with the R2 absent. For the case where the R2 current system is set to 30º, the AU

341   and AL indices for the Northern and Southern ionospheres are respectively: 2619, 2554, -2911,

342   and -2877 nT. For the case, where R2 currents system is set to 32º, the AU and AL indices are:

343   2131, 2071, -2345, -2315 nT. For R2 set to 34º, the indices are: 1765, 1708, -1899, -1871 nT.

344   The results for the equivalent currents for the case where R2 currents system is set to 32º are

345   presented in the Figure 11. The results for the setup with the R2 absent are shown in the Figure

346   12. In this case, the westward electrojet in the midnight sector in strong in magnitude. For the

347   same potential drop as in the previous cases, we obtained the AU and AL indices for the

348   Northern and Southern ionospheres respectively: 1376, 1315, -1192, and -1189 nT, which is

349   close to the indices observed around 09:10 UT. We also performed a simulation for the increased

350   potential drop and the results are shown in the Figure 12. The potential difference increased up to

351   222 kV (from -79 to 143 kV) did not improve the agreement with the observed AU and AL

352   indices, which are respectively 1789, 1709, -1549, and -1546 for the Northern and Southern

353   ionospheres. The further increase in this difference also did not improve the comparison

354   significantly.

355   To summarize the results of the Figures 11 and 12, we conclude that for the event of April

356   5, 2010 for the northern hemisphere, the SuperMAG observations agree better with the run

357   where R2 currents are absent. Indeed, the observed electrojet signatures are weak in the morning

358   sector and strong in the post-midnight sector, as predicted in the Figure 12 (left panel). The result

359   is also consistent with AMPERE observations in the northern hemisphere where the R2 currents

360   are weak near 09:10 UT. For the southern hemisphere the situation is more complex. The

361   AMPERE data shows a relatively strong R2 system, thus demonstrating a strong asymmetry

362   between two hemispheres that the L-2015 model cannot predict. This is probably because the

363   current version of the L-2015 model does not take into account all mechanisms that produce

364   asymmetry between two hemispheres, for example the potential drop difference along the field

365   line for the auroral zone, and the asymmetry due to IMF By. The SuperMAG data is scarce but

366   there is a clear signature of an enhanced electrojet in the morning sector, which is consistent with

367   the result of the run with R2 in the Figure 11 (right panel). We conclude therefore that the

368   asymmetry observed in the electrojet magnitude between two hemispheres is explained by the

369   asymmetry in the R2 distribution, and predicted by the L-2015 model, if the L-2015 results are

370   analyzed for each hemisphere separately.

371   Figure 13 shows the simulated magnetic field that would be measured on the ground in

372   various magnetic local time (MLT) sectors of the auroral zone for the runs described above. The

373   multicolored curves show the result of the simulation made for the cases, where the location in

374   colatitude of the R2 currents was set to $30°$ (red line), $32°$ (blue), and $34°$ (green). The solid black

375   curve shows the simulation result for the case, where R2 is absent from the model setup but all

376   other parameters are the same as above. The black dotted curves show the cases where the R2 is

377   absent and the electric potential drop over the polar cap is increased to 222 kV, and the black

378   dashed curves show the results with an increased potential drop up to 273 keV. The observed

379   AU/-AL is approximately 1000 nT (Figure 8), therefore we conclude that the run without R2

380 agrees better with the magnetometer observations in the northern hemisphere, where the stations

381 for AU/AL indices are located. As noted above, the L-2015 model predicts that for the southern

382 hemisphere, where the R2 system is present in the AMPERE data, the agreement would be better

383 with the R2 setup, and would produce stronger AU/AL signatures. Currently, this is difficult to

384 verify as no AU/AL index is available for the Southern hemisphere.

385 **3. Discussion and Conclusion**

386 Modern global coupled models of the Geospace show highly complex, self-consistent and

387 interconnected interactions between field-aligned currents and their ionospheric closures.

388 Because of the complexity, cause and effect relationships are sometimes hidden in a global self-

389 consistent solution. In this study, we demonstrated how the simple model of ionospheric

390 electrodynamics could help unravel some important aspects of the effect of R2 currents on the

391 entire auroral oval.

392 Generating multiple simulations, we have selected a few for this demonstration. The

393 effects of R2 currents on the auroral ionosphere are confirmed by multiple numerical

394 experiments. The main results could be summarized as follows:

395 1. A strong R2 current provides a robust closure for ionospheric currents originating from

396 R1 via the auroral zone ionosphere. Since the conductivity of the magnetic field lines is much

397 higher than the ionospheric conductivity, the availability of the connection via R2 current can

398 drastically change the parameters of the auroral zone: ionospheric and field-aligned currents,

399 magnetic fields measured on the ground, and auroral indices. In the model, the larger magnitude

400 westward auroral electrojet is found to be in the day-to-dawn sector, while the ionospheric and

401 equivalent ionospheric currents on the night side have a much lower magnitude.

402   2. The location of R2 currents also affects the distribution of ionospheric and equivalent

403   currents, as well as ground magnetic field measurements. As the distance between the current

404   systems R1 and R2 increases, the magnitude of ionospheric currents decreases as the ionospheric

405   currents propagate to larger regions at lower latitudes.

406   3. When R2 current cannot provide proper closure, the night side ionospheric currents

407   increase in magnitude. Therefore, the R1 current is closed via ionosphere of the auroral oval

408   night side. Ionospheric currents flow from dawn to dusk over the night-side ionosphere. The

409   simulations show the appearance of the westward auroral electrojet in the night region of the

410   auroral zone in case of absent R2 currents.

411   4. For the case of 21:10 UT of April 6, we found that to obtain the equivalent currents of

412   the magnitude registered by ground magnetometers shown by SuperMAG, the potential drop

413   over the polar cap in the model should be greater to that suggested by AMPERE products.

414   5. For the case of 09:10 UT of April 5, we found that for the northern hemisphere, the

415   SuperMAG data shows strong currents in the area from dusk to midnight, which agrees well with

416   the results for the model run without R2 current. For the southern hemisphere, SuperMAG data

417   shows strong currents in the MLT ~06 h sector. This characteristic is reproduced by the run with

418   R2 located at 32º magnetic colatitude. AMPERE data are in agreement with the model results,

419   showing a weak R2 system in northern hemisphere and a visible R2 system in southern

420   hemisphere.

421

422   It should be noted that the substorm current wedge is not included in our model, and we

423   have studied the characteristics of the auroral zone currents without considering the additional

424   system of currents forming the substorm current wedge. AMPERE data does not show any

425 additional current systems adjacent to R1 currents that could be indicative of an intense substorm

426 current wedge for two considered events, therefore justifying our approach. We anticipate that

427 substorm current wedge could affect the results, and consider this effect in the future works.

428

429   We demonstrated that a part of the night side westward electrojet could only appear if R2

430 currents are weak or absent. Still, the magnitude of the equivalent ionospheric current on the

431 night side is less than observed, if the model uses the electric potential derived from the

432 AMPERE products. It suggests that either potential drop over the polar cap is greater than that

433 proposed by the AMPERE group, or some additional factors, such as substorm current wedge,

434 the potential drop along the field line, or errors in the specification of auroral conductivity as a

435 function of Kp index. The clarification of these uncertainties will be the subject of future work.

436

4. Acknowledgements:

5. References

Anderson, B. J. et al. (2008a), Statistical Birkeland current distributions from magnetic field observations by the Iridium constellation, Annales Geophys., 26, 671-687, doi:10.5194/angeo-26-671-2008.

Anderson, B. J., H. Korth, C. L . Waters, D.L.Green,V.G.Merkin,R.J.Barnes, and L. P. Dyrud (2014), Development of large-scale Birkeland currents determined from the Active Magnetosphere and Planetary Electrodynamics Response Experiment, Geophys. Res. Lett., 41, 3017–3025, doi:10.1002/2014GL059941.

Akasofu, S.-I. (1964), The Development of The Auroral Substorm. Planet. Space Sci. vol. 12, issue 4, 273-282, doi: 10.1016/0032-0633(64)90151-5.

Amm, O., and A. Viljanen (1999), Ionospheric disturbance magnetic field continuation from the ground to the ionosphere using spherical elementary current systems, Earth Planets Space, 51, 431–440.

Anderson, B. J., S.-I. Ohtani, H. Korth, and A. Ukhorskiy (2005), Storm time dawn-dusk asymmetry of the large-scale Birkeland currents, J. Geophys. Res., 110, A12220, doi:10.1029/2005JA011246.

Anderson, B. J., Olson, C. N., Korth, H., Barnes, R. J., Waters, C. L., & Vines, S. K. (2018). Temporal and spatial development of global Birkeland currents. Journal of Geophysical Research: Space Physics,123, 4785–4808. https://doi.org/10.1029/2018JA025254

Bartels, J. (1949) - The standardized index Ks and the planetary index Kp, IATME Bulletin 12b, 97.

491   Benkevich, L., and W. Lyatsky (2000), Detached vortices in equivalent ionospheric currents

492   in the winter dayside ionosphere, Geophys. Res.Lett., 27(9), 1375–1378,

493   doi:10.1029/1999GL003711.

494   Benkevich, L., W. Lyatsky, and L. L. Cogger (2000), Field-aligned currents between

495   conjugate hemispheres, J. Geophys. Res., 105(A12), 27,727–27,737,

496   doi:10.1029/2000JA900095.

497   Buzulukova, N., M.-C. Fok, T. E. Moore, and D. M. Ober (2008), Generation of

498   plasmaspheric undulations, Geophys. Res. Lett.,35, L13105, doi:10.1029/2008GL034164.

499   Connors, M., C. T. Russell, and V. Angelopoulos (2011), Magnetic flux transfer in the 5

500   April 2010 Galaxy 15 substorm: An unprecedented observation, Ann. Geophys., 29, 619–622,

501   doi:10.5194/angeo−29−619−2011.

502   Davis, T. N., and M. Sugiura (1966), Auroral electrojet activity index AE and its universal

503   time variations, J. Geophys. Res., 71, 785–801.

504   Fok, M.−C., Buzulukova, N., Chen, S.−H., Valek, P. W., Goldstein, J., and McComas, D. J.

505   (2010), Simulation and TWINS observations of the 22 July 2009 storm, *J. Geophys. Res.*, 115,

506   A12231, doi:10.1029/2010JA015443.

507   Fukushima, N. (1976), Generalized theorem for no ground magnetic effect of vertical

508   currents connected with Pedersen currents in the uniform-conductivity ionosphere, Rep. Ionos.

509   Space Res. Japan, 30, 35–40.

510   Ganushkina, N. Y., Liemohn, M. W., & Dubyagin, S. (2018). Current systems in the Earth's

511   magnetosphere. Reviews of Geophysics, 56, 309–332. Doi:10.1002/2017RG000590

512   Gjerloev, J. (2012), The SuperMAG data processing technique, J. Geophys. Res., 117,

513   A09213, doi:10.1029/2012JA017683.

514   Hajra, R., Echer, E., Tsurutani, B. T., and Gonzalez, W. D.: Solar cycle dependence of

515   High-Intensity Long-Duration Continuous AE Activity (HILDAA) events, relativistic electron

516   predictors?, J. Geophys. Res., 118, 5626–5638, https://doi.org/10.1002/jgra.50530, 2013.

517   Iijima, T., and T. A. Potemra (1976), The amplitude distribution of field-aligned currents at

518   northern high latitudes observed by TRIAD, J. Geophys. Res., 81, 2165–2174,

519   doi:10.1029/JA081i013p02165.

520   Jaggi, R. K., and R. A. Wolf (1973), Self-consistent calculation of the motion of a sheet of

521   ions in the magnetosphere, J. Geophys. Res., 78, 16,2852–16,2866.

522   Hardy, D. A., M. S. Gussenhoven, R. Raistrick, and W. J. McNeil (1987), Statistical and

523   functional representations of the pattern of auroral energy flux and conductivity, J. Geophys.

524   Res., 92, 12,275–12,294, doi:10.1029/JA092iA11p12275.

525   Kamide, Y., A. D. Richmond, and S. Matsushita (1981), Estimation of ionospheric electric

526   fields, ionospheric currents, and field-aligned currents from ground magnetic records, J.

527   Geophys. Res., 86, 801–813, doi:10.1029/JA086iA02p00801.

528   Kepko, L., McPherron, R.L., Amm, O. et al. Space Sci Rev (2015) Substorm Current Wedge

529   Revisited. 190: 1. doi:10.1007/s11214-014-0124-9

530   Lyatskaya, S., W. Lyatsky, and G. V. Khazanov (2014), Effect of interhemispheric field-

531   aligned currents on the region 1 currents, Geophys. Res. Lett., 41, 3731-3737,

532   doi:10.1002/2014GL060413.

533   Lyatskaya, S., G. V. Khazanov, and E. Zesta (2015), Interhemispheric field-aligned currents:

534   Simulation results, J. Geophys. Res. Space Physics, 119, 5600-5612,

535   doi:10.1002/2013JA019558.

536   Lyatskaya, S., W. Lyatsky, and E. Zesta (2016), Effect of interhemispheric currents on

537   equivalent ionospheric currents in two hemispheres: Simulation results, J. Geophys. Res. Space

538   Physics, 121, doi:10.1002/2015JA021167.

539   Lyatsky, W., and Y. P. Maltsev (1983), Magnetosphere-Ionosphere Interaction, Nauka,

540   Moscow.

541   Lyatsky, W. B., Y. P. Malsev, and S. V. Leontyev (1974), Three-dimensional current system

542   of magnetic substorm, Planet. Space Sci., 22, 1231–1247.

543   Maltsev, Y. P. (1974), The effect of ionospheric conductivity on the convection system in

544   the magnetosphere, Geomagn. Aeron., 4, 128.

545   Matsushita, S., and W.-Y. Xu (1982), Equivalent ionospheric current systems representing

546   IMF sector effects on the polar geomagnetic field, Planet. Space Sci., 30(7), 641–656,

547   doi:10.1016/0032-0633(82)90025-3.

548   Murphy, K. R., I. R. Mann, I. J. Rae, C. L. Waters, H. U. Frey, A. Kale, H. J. Singer, B. J.

549   Anderson, and H. Korth (2013), The detailed spatial structure of field-aligned currents

550   comprising the substorm current wedge, J. Geophys. Res. Space Physics, 118, 7714–7727,

551   doi:10.1002/2013JA018979.

552   Ohtani, S., S. Wing, P. T. Newell, and T. Higuchi (2010), Locations of night−side

553   precipitation boundaries relative to R2 and R1 currents, J. Geophys. Res., 115, A10233,

554   doi:10.1029/2010JA015444

555   Papitashvili, V. O., F. Christiansen, and T. Neubert (2002), A new model of field-aligned

556   currents derived from high-precision satellite magnetic field data, Geophys. Res. Lett., 29(14),

557   1683, doi:10.1029/2001GL014207.

558   Sazykin, S., R. A. Wolf, R. W. Spiro, T. I. Gombosi, D. L. De Zeeuw, and M. F. Thomsen,

559   (2002), Interchange instability in the inner magnetosphere associated with geosynchronous

560   particle flux decreases, Geophys. Res. Lett., 29(10), doi: vol. 29, issue 10, doi:

561   10.1029/2001GL014416, 2002

562   Toffoletto, F., Sazykin, S., Spiro, R. et al. Space Science Reviews (2003) 107: 175.

563   https://doi.org/10.1023/A:1025532008047

564   Tomita, S., M. Nose, T. Iyemori, H. Toh, M. Takeda, J. Matzka, G. Bjornsson, T.

565   Saemundsson, A. Janzhura, O. Troshichev, and G. Schwarz. Magnetic local time dependence of

566   geomagnetic disturbances contributing to the AU and AL indices. doi:10.5194/angeo-29-673-

567   2011

568   Tsurutani, B. T., Verkhoglyadova, O. P., Lakhina, G. S., and Yagitani, S. (2009), Properties

569   of dayside outer zone chorus during HILDCAA events: Loss of energetic electrons, *J. Geophys.*

570   *Res.*, 114, A03207, doi:10.1029/2008JA013353

571   Waters, C. L., J. W. Gjerloev, M. Dupont, and R. J. Barnes (2015), Global maps of ground

572   magnetometer data, J. Geophys. Res. Space Physics, 120, doi:10.1002/2015JA021596

573   Weygand, J. M., O. Amm, V. Angelopoulos, S. E. Milan, A. Grocott, H. Gleisner, and C.

574   Stolle (2012), Comparison between SuperDARN flow vectors and equivalent ionospheric

575   currents from ground magnetometer arrays, J. Geophys. Res., 117, A05325,

576   doi:10.1029/2011JA017407.

577   Weimer, D. R. (2001), Maps of ionospheric field-aligned currents as a function of the

578   interplanetary magnetic field derived from Dynamics Explorer 2 data, J. Geophys. Res., 106,

579   12,889–12,902, doi:10.1029/2000JA000295.

580   Yu, Y., J. Cao, H. Fu, H. Lu, and Z. Yao (2017), The effects of bursty bulk flows on global-

581   scale current systems, J. Geophys. Res. Space Physics, 122 , 6139–6149,

582   doi:10.1002/2017JA024168.

583   Zheng, Y., A. T. Y. Lui, M.-C. Fok, B. J. Anderson, P. C. Brandt, T. J. Immel, and D. G.

584   Mitchell (2006), Relationship between Region 2 field-aligned current and the ring current:

585   Model results, J. Geophys. Res., 111, A11S06, doi:10.1029/2006JA011603.

586
587
588

589   **6. Figures**
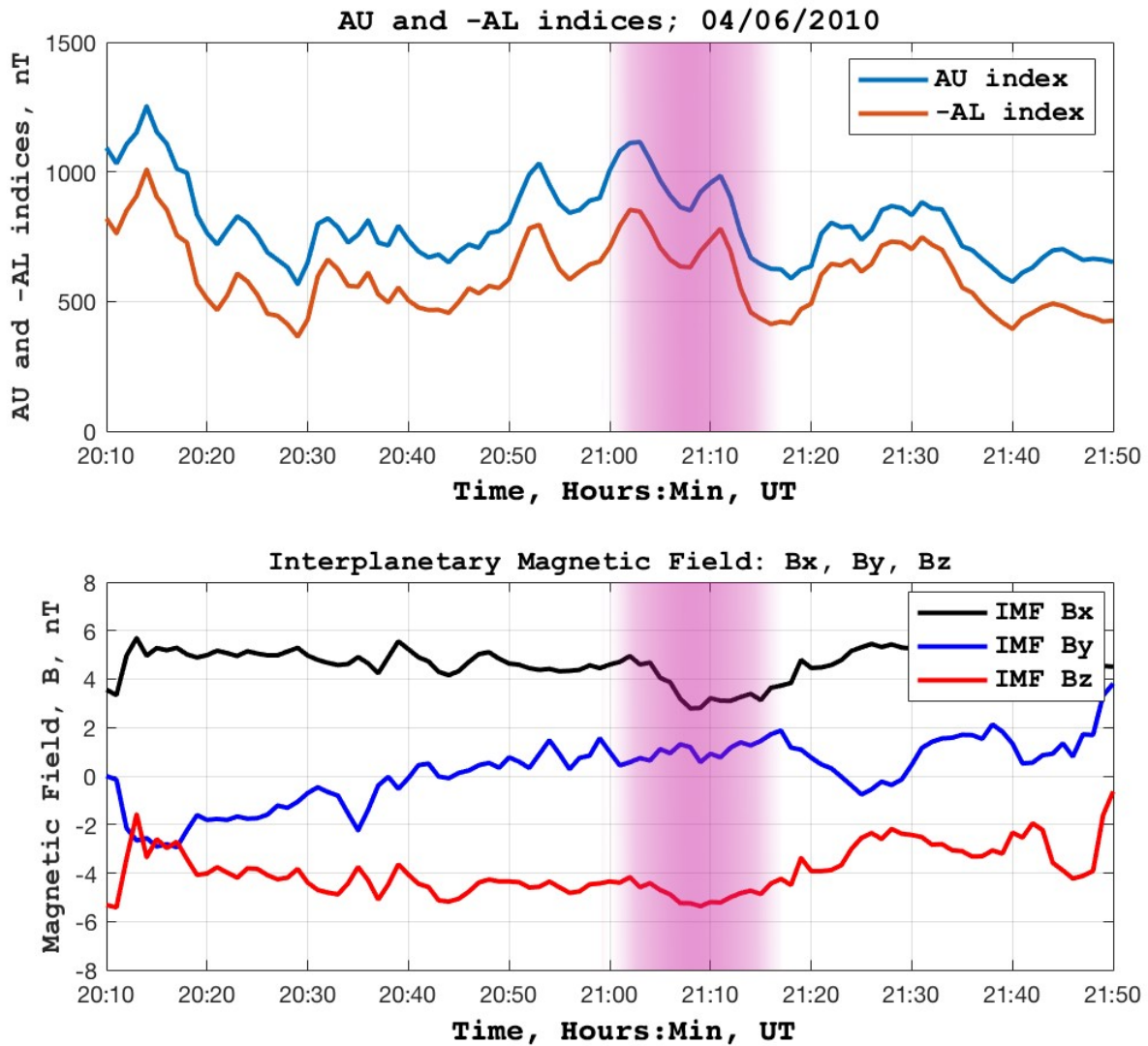
590
591
592   **Figure 1.** Top panel shows the AU and negative AL indices for April 06, 2010 from
593   approximately 20:00 UT to 22:00 UT. The AU index is shown in blue and negative AL is shown
594   in red. The lower panel shows the parameters of the interplanetary magnetic field (IMF): Bx
595   (black), By (blue), and Bz (red). The pink shade indicates an interval of interest around 21:10
596   UT.

597
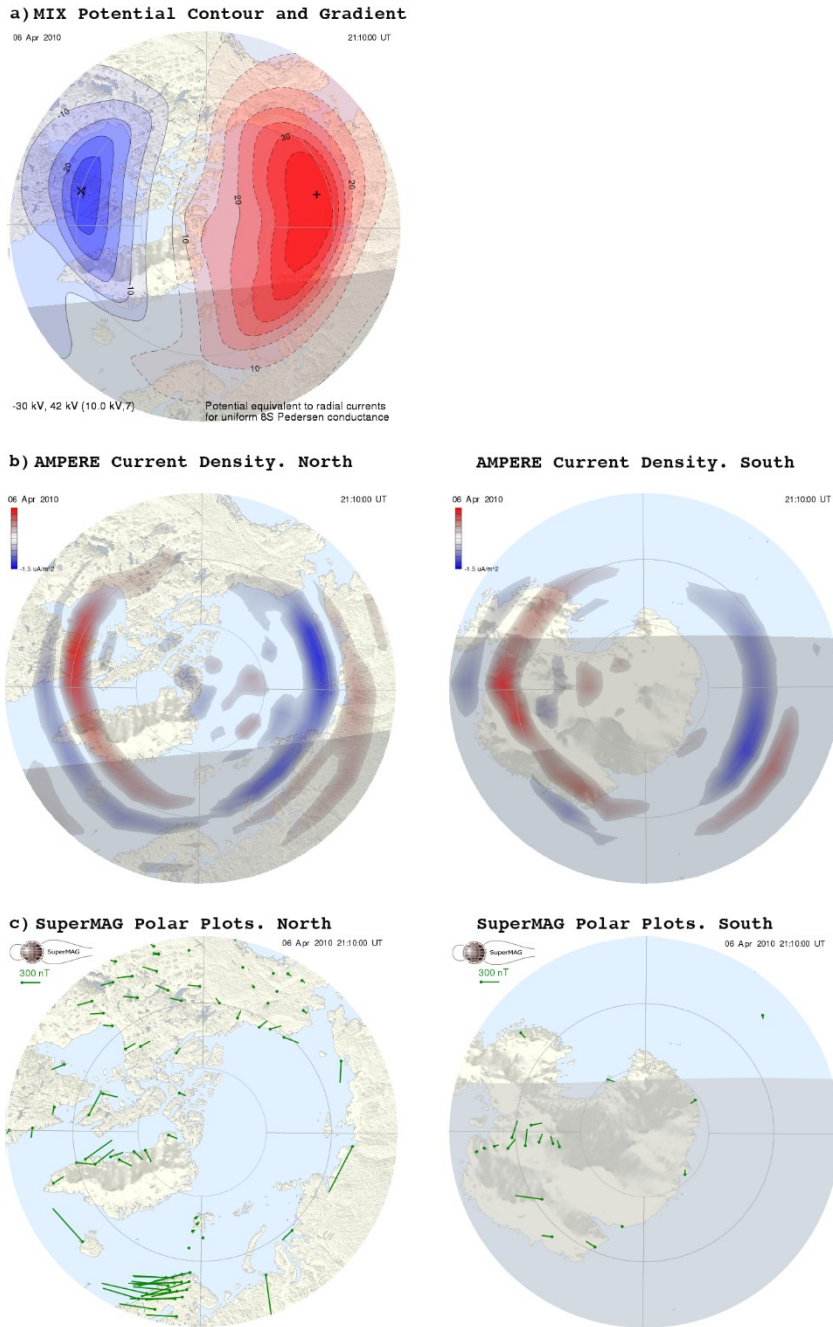
Figure 2. The electric potential (a) and field-aligned current density (b) from AMPERE data for April, 06, 2010, 21:10 UT. SuperMAG polar plots (c) with ground magnetometers vectors, which represent equivalent ionospheric currents for the northern (left) and southern (right) hemisphere for the same time. The southern hemisphere is shown as a mirrored image. The direction toward the Sun is above each plot, and towards dawn (06 MLT) is to the right. The enhanced electrojet region in the midnight sector is seen in panel (c) for the northern hemisphere.

604

605

Potential Distribution in the Polar Cap, kV

606
607
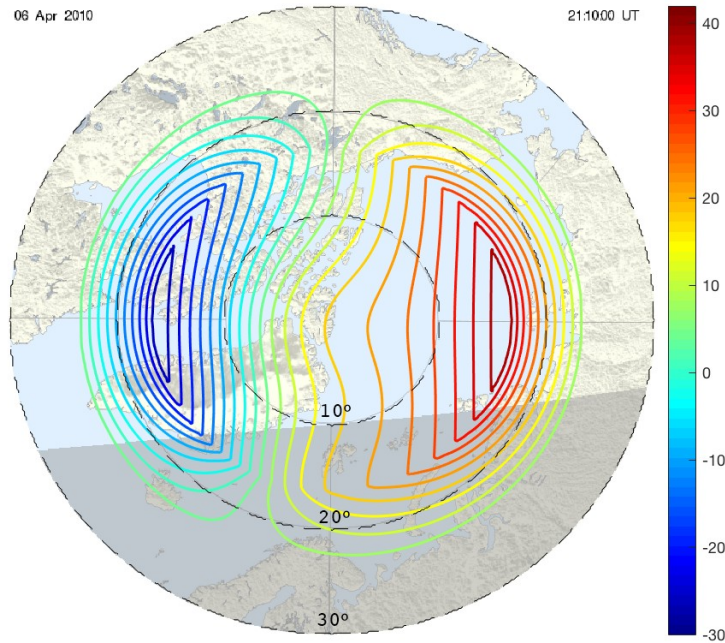
608   **Figure 3.** The electric potential simulated with the L-2015 model for April 06, 2010, 21:10 UT.
609   The parameters of the simulated event are: R1 current is located at 18° of colatitude, R2 current
610   is at 26°. The auroral precipitation parameters are typical for KP = 4. The electric potential
611   changes from -30 kV at the western boundary of the polar cap (18 MLT) to +42 kV at the eastern
612   boundary (06 MLT) as shown in the Figure 2 (a).
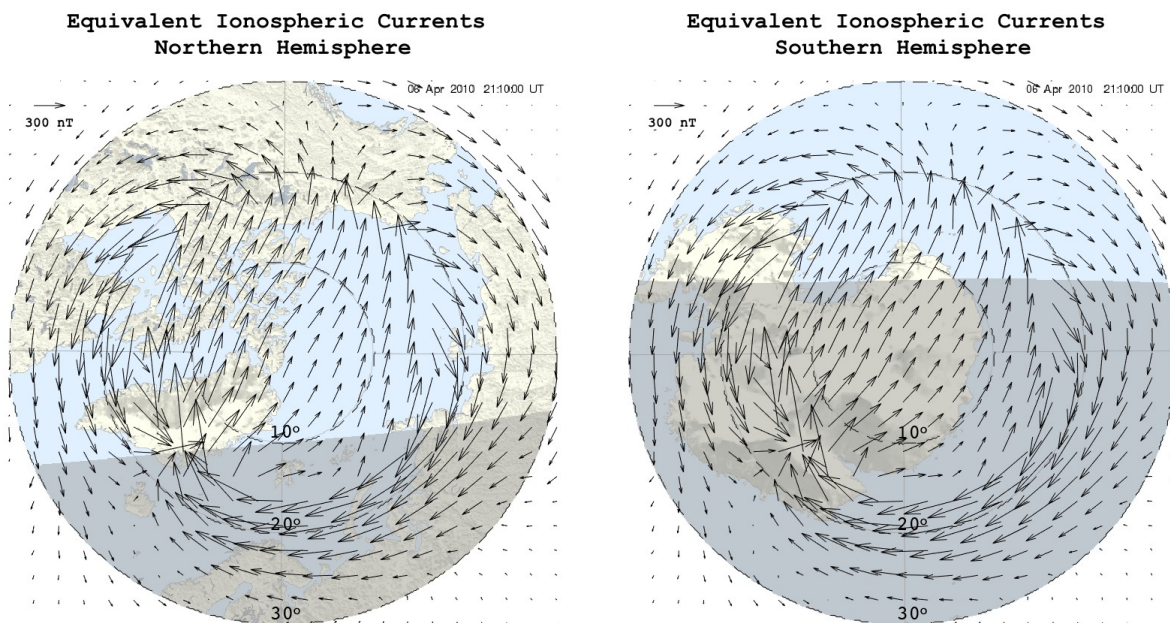
613

614

615
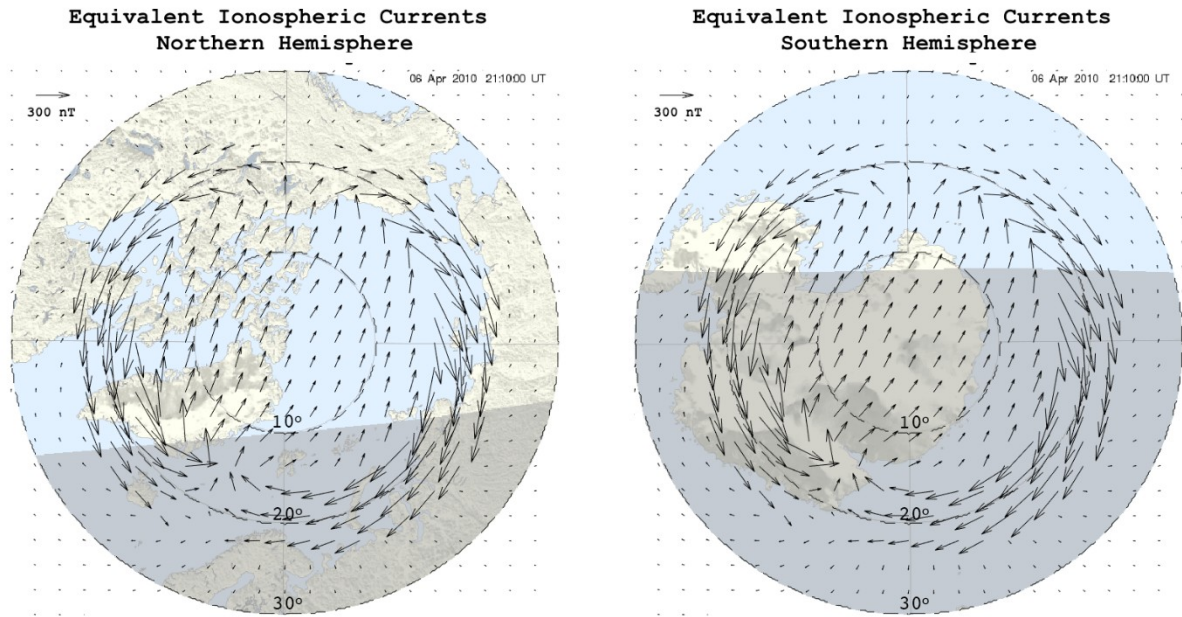
616   **Figure 4.** The simulated equivalent ionospheric currents, for the Northern (left) and Southern
617   (right) hemispheres for the case 1, where R1 currents are located at 18º colatitude; R2 currents at
618   26º; the ionospheric conductivity produced by geomagnetic activity is typical for KP=4, e.g. the
619   maxima of Pedersen and Hall conductivities are 10.0 S and 18.0 S respectively. The electric
620   potential changes from -30 kV at the western boundary of the polar cap (18 MLT) to +42 kV at
621   the eastern boundary (06 MLT) as taken from the Figure 2 (b). The Southern hemisphere is
622   shown as a mirrored image. Here and further, the direction to the Sun (12 MLT) is above each
623   image; the direction of dawn (06 MLT) is to the right. Note the absence of an electrojet near the
624   midnight sector in the distribution of equivalent currents.

625
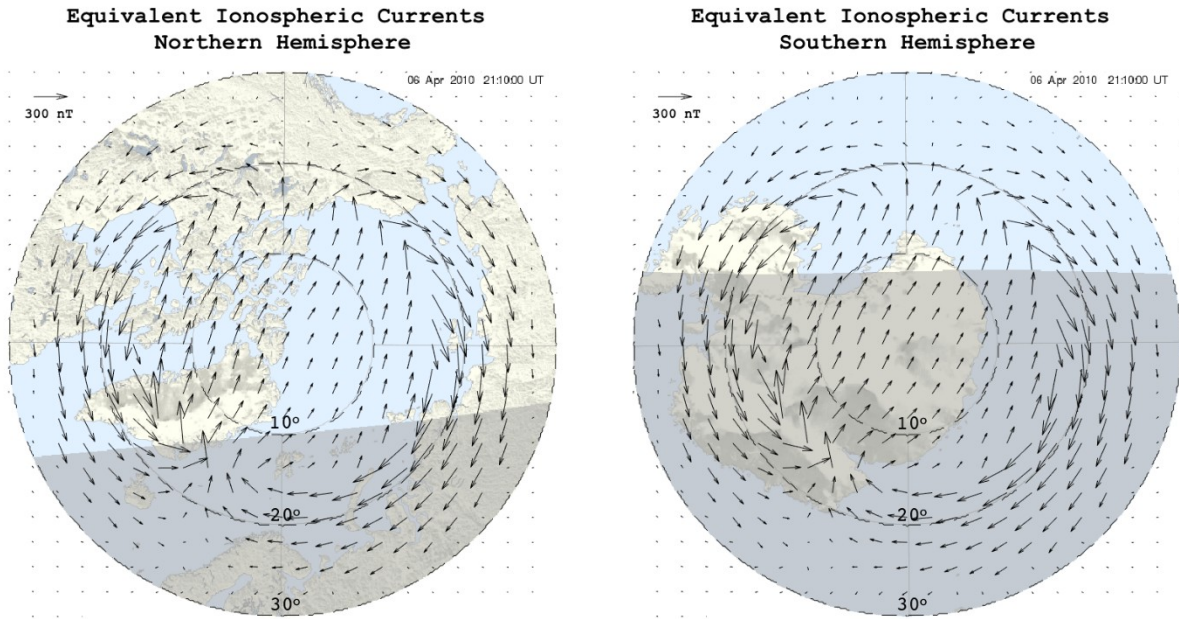
Figure 5. The simulated equivalent ionospheric currents, for the Northern (left) and Southern (right) hemispheres for the case 2, where R1 currents are located at 18° colatitude; R2 currents at 30°. The electric potential changes from -30 kV at the western boundary of the polar cap (18 MLT) to +42 kV at the eastern boundary (06 MLT). Note the absence of the electrojet near the midnight sector.

633

634

Figure 6. The simulated equivalent ionospheric currents, for the Northern (left) and Southern
(right) hemispheres for the case of negligible R2 currents and an increased electric potential drop
across the polar cap. The potential drop for the simulation is set to 180 kV, from -75 to +105 kV.
All other parameters of the simulation are the same. Note the appearance of the intense electrojet
near the midnight sector.

640
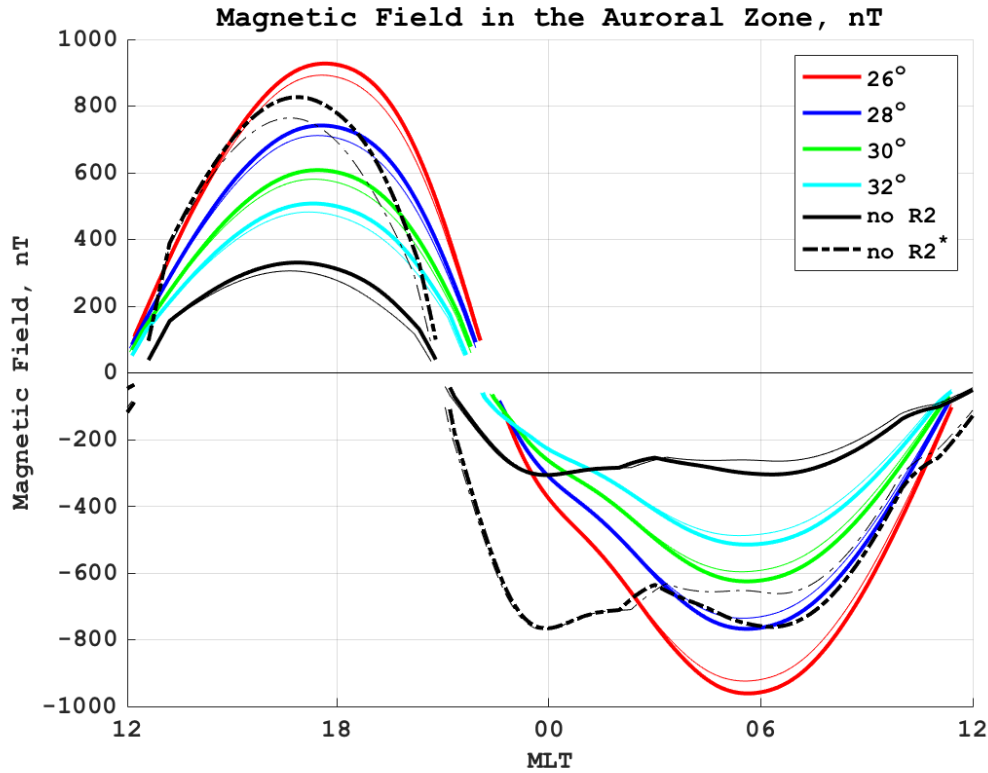
Figure 7. The simulated magnetic field that would be measured on the ground in various magnetic local time (MLT) sectors in the area between R1 and R2 currents for the cases described above. In case of absence of R2 currents, the auroral zone width is set to 12º below R1 current. The multicolored curves show the result of the simulation made for the cases with the R2 currents set at 26º (red line), (Figure 4), 28º (blue), 30º (green), (Figure 5), and 32º (cyan). The solid black curve shows the simulation result for the case where R2 is absent from the model setup but all other parameters are the same as above. The black dashed curve shows the case with the R2 is absent and electric potential drop over the polar cap is increased and set to 180 kV, from -75 to +105 kV (Figure 6). The bold lines show the magnitude of the magnetic field in the Northern hemisphere, thin lines show the results for the Southern hemisphere. As the simulation is made for the spring season, the difference between the magnitudes for the two hemispheres is negligible. The positive magnetic field is caused by eastward auroral electrojet; its maximum represents AU index. The negative magnetic field is caused by westward auroral electrojet, its minimum represents AL index for the time given. Note that currently measurements of AE indices are available only for the Northern hemisphere.
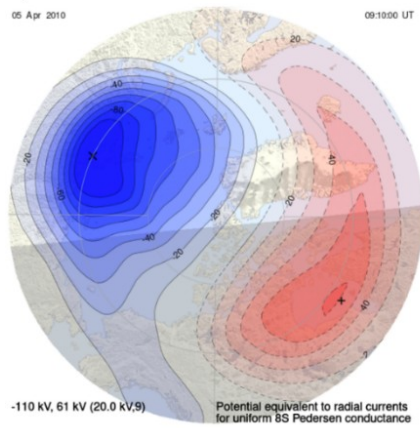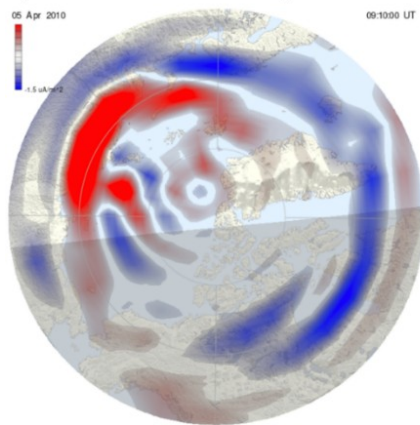
658
659
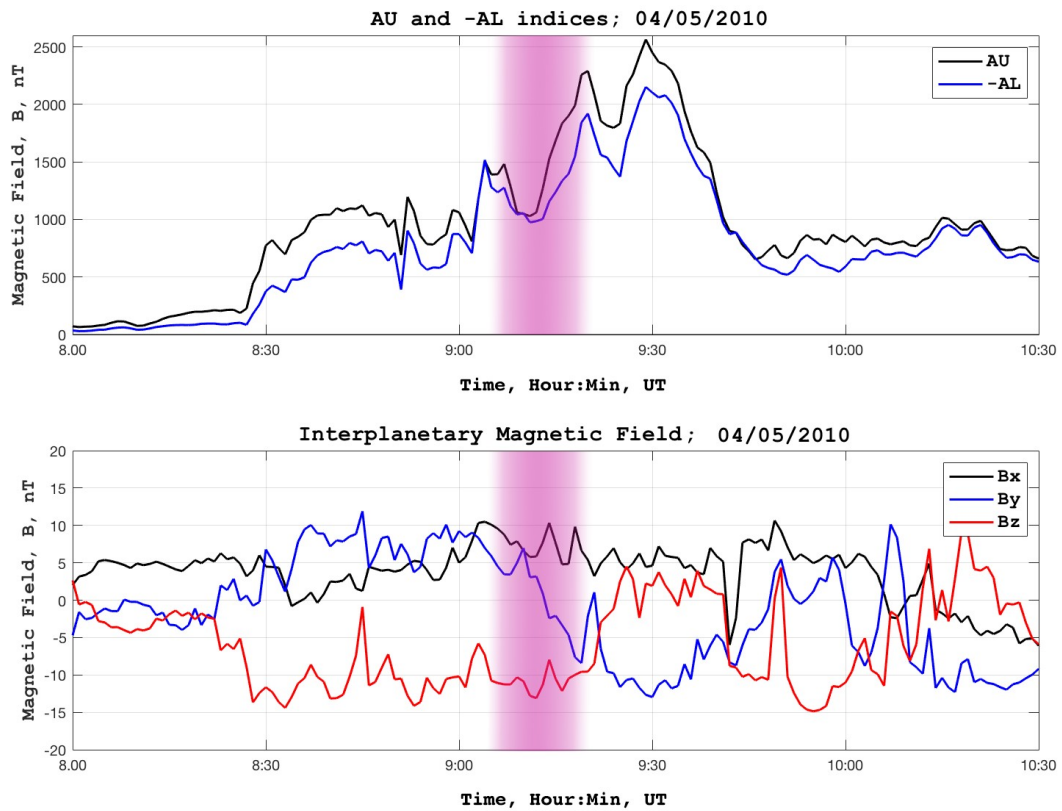
Figure 8. The top panel shows the AU and negative AL indices for the morning hours for April
05, 2010. The AU index is shown in black and negative AL is shown in blue. The lower panel
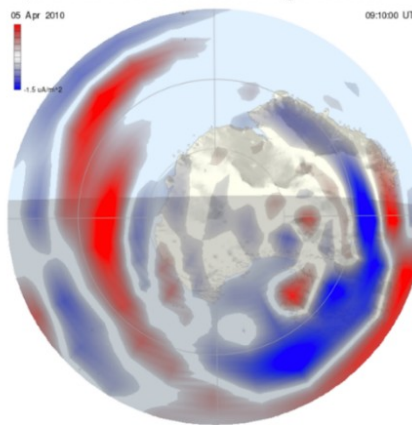shows the parameters of the interplanetary magnetic field: Bx (black), By (blue), and Bz (red).

663

664
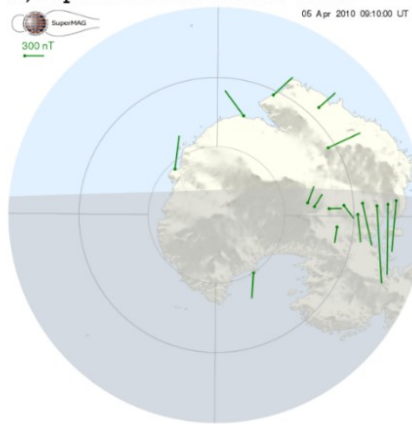
Figure 9. The electric field potential (a) and the field-aligned current density (b) derived from
AMPERE data for April 05, 2010, 9:10 UT. SuperMAG polar plots (c) with ground
magnetometers vectors, which represent equivalent ionospheric currents for the Northern (left)
and Southern (right) hemisphere for the same time. The Southern hemisphere is shown as a
mirrored image.

670

671

672

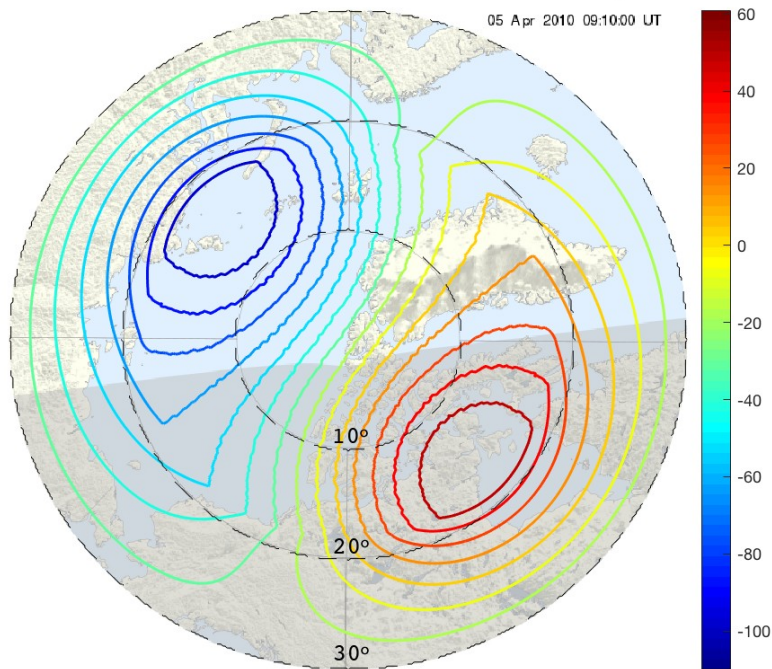Potential Distribution in the Polar Cap, kV

673

674 **Figure 10.** The simulated electric potential for April 5 2010, 9:10 UT with the L-2015 model.

675 The parameters of the simulated case are: R1 current is located at 20º of colatitude, R2 current is

676 at 30º. The auroral precipitation parameters are typical for KP = 5; the maxima of Pedersen and

677 Hall conductivities are 12.5 S and 25.9 S respectively. The electric potential difference for the

678 boundary conditions simulation changes from -110 kV at the western boundary of the polar cap

679 to +61 kV at the eastern boundary, but the maximum and minimum of a potential shifted from 06

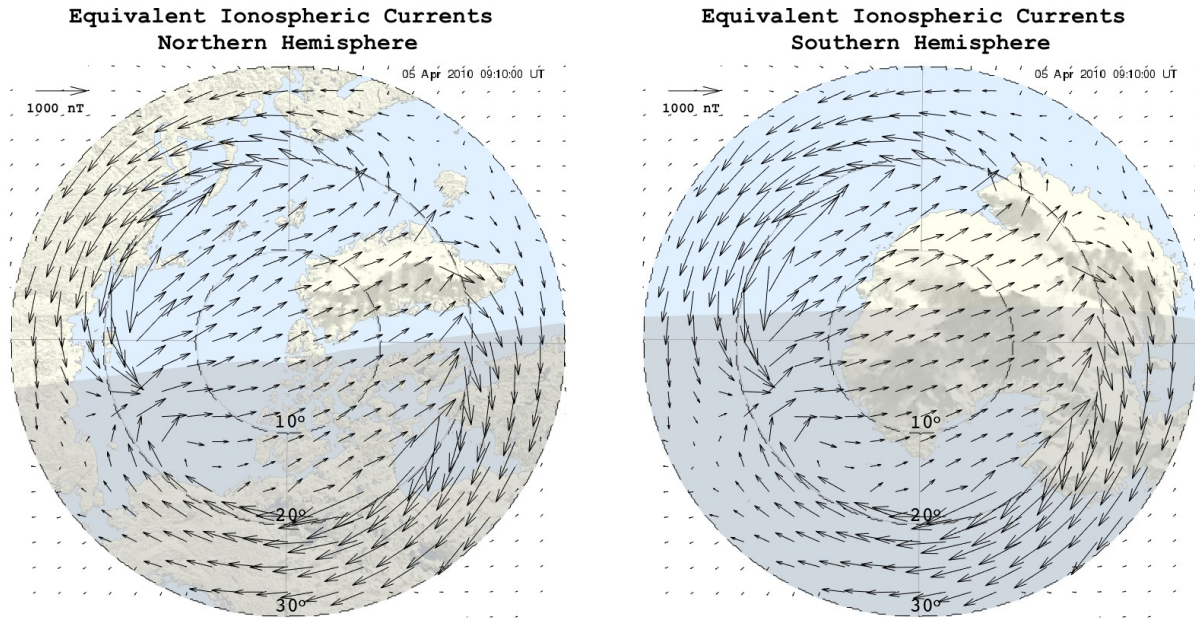680 and 18 MLT to 03 and 15 MLT respectively due to By effect.

681

682
683 **Figure 11.** The simulated equivalent ionospheric currents, for the Northern (left) and Southern
684 (right) hemispheres for the case, in which R1 currents are located at 20º colatitude; R2 currents at
685 32º; the ionospheric conductivity is typical for KP=5. The electric potential difference for the
686 boundary conditions simulation changes from -110 kV at the western boundary of the polar cap
687 to +61 kV at the eastern boundary as in Figure 10. Note that the reference vector for the images
688 is set at 1000 nT.
689
690

691

692

**Equivalent Ionospheric Currents
Northern Hemisphere**

**Equivalent Ionospheric Currents
Southern Hemisphere**

693
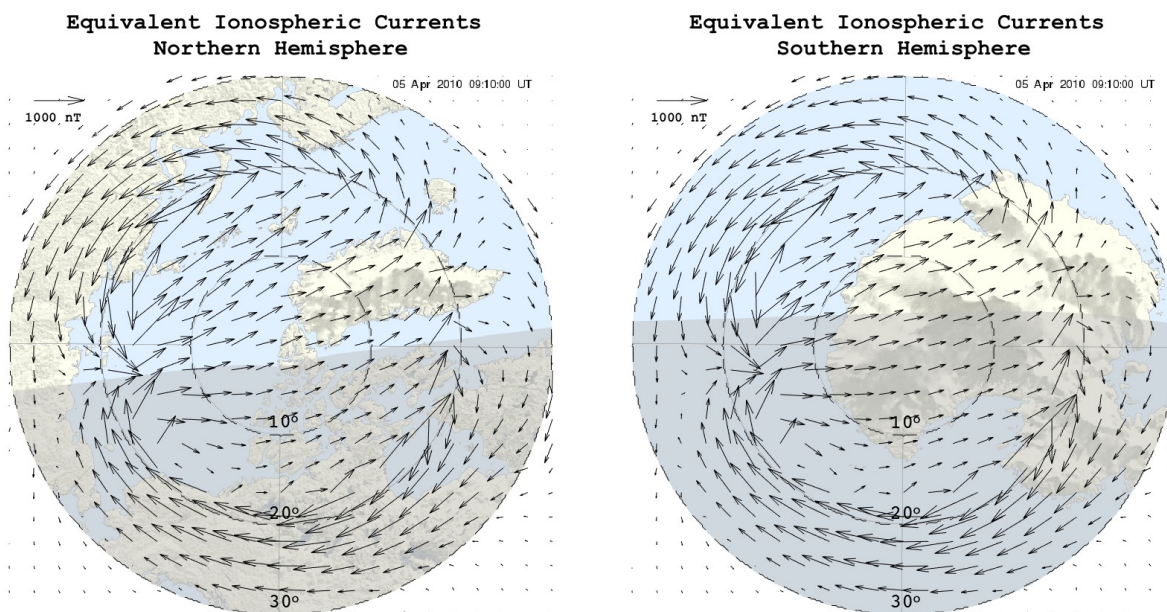
694 **Figure 12.** The simulated equivalent ionospheric currents, for the Northern (left) and Southern

695 (right) hemispheres for the case of negligible R2 currents, while all other simulation parameters

696 are the same as in Figure 11. R1 currents are located at 20º colatitude, the ionospheric

697 conductivity is typical for KP=5. The electric field potential difference for the boundary

698 conditions simulation changes from -110 kV at the western boundary of the polar cap to +61 kV

699 at the eastern boundary.

700

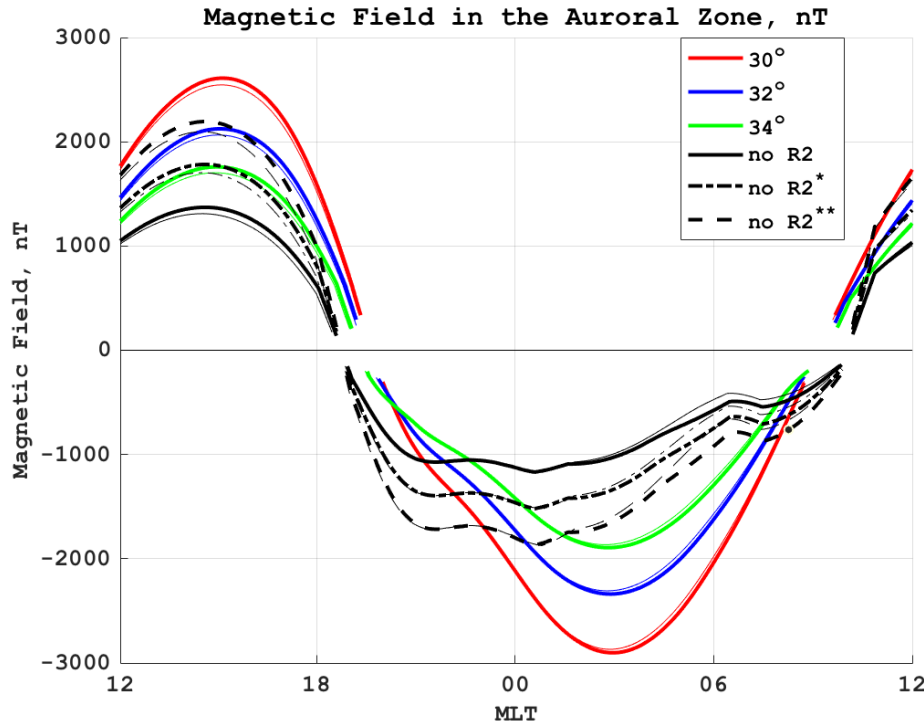**Magnetic Field in the Auroral Zone, nT**

701

702

Figure 13. The simulated magnetic field which would be measured on the ground in different
magnetic local time (MLT) sectors of the auroral zone for the case of April 05, 2010, 09:10 UT,
for the model runs described above. The multicolored curves show the results of the simulation
made for the cases with the R2 currents set to 30º (red line), 32º (blue), and 34º (green). The solid
black curve shows the results for the case where R2 is absent from the model setup but all other
parameters are the same as above. The black dash-dotted curve shows the results for the case
with the R2 absent and the electric potential drop increased by 30% compared to the original
case, up to 222 kV (from -143 to 79 kV). The black dashed curve shows the results for the run
with the R2 absent and the potential drop increased by 60%, up to 273 kV (from -176 to +97
kV). The bold lines indicate the Northern hemisphere fields magnitude, with thin lines for the
Southern hemisphere. The positive magnetic field is caused by eastward auroral electrojet; its
maximum represents AU index for each hemisphere for the given time. The negative magnetic
field is caused by westward auroral electrojet; its minimum represents AL index. The observed
values for AU/-AL of ~1000 nT near 09:10 UT for the northern hemisphere agree well with the
run without R2 currents.

718

719

720